Journal of Energy Storage 38 (2021) 102508

Contents lists available at ScienceDirect

Journal of Energy Storage

journal homepage: www.elsevier.com/locate/est

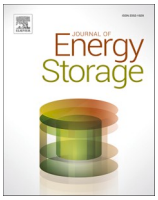

# A superconducting magnetic energy storage with dual functions of active filtering and power fluctuation suppression for photovoltaic microgrid

Jian Xun Jin [a], Jian Wang [a], Ruo Huan Yang [a], Tian Long Zhang [a], Shuai Mu [a], Ying Jun Fan [a], Yun Qi Xing [b,*]

[a] School of Electrical and Information Engineering, Tianjin University, Tianjin 300072, China
[b] State Key Laboratory of Reliability and Intelligence of Electrical Equipment, Hebei University of Technology, Tianjin 300132, China

ARTICLE INFO

*Keywords:*
Superconducting magnetic energy storage (SMES)
Shunt active power filter (SAPF)
Photovoltaic microgrid
Multi-objective control
Fuzzy logic control (FLC)

ABSTRACT

This paper proposes a superconducting magnetic energy storage (SMES) device based on a shunt active power filter (SAPF) for constraining harmonic and unbalanced currents as well as mitigating power fluctuations in photovoltaic (PV) microgrid. The AC side of the SAPF is interfaced to the point of common coupling (PCC), and its DC-link is with integration of a DC/DC converter and an energy storage superconducting coil (SC). A multi-objective control technique based on modified $i_p - i_q$ method and hysteresis SVPWM is adopted to implement the dual functions of active filtering and power fluctuation suppression. A fuzzy logic control (FLC) method is proposed for the DC/DC converter to stabilize the DC-link voltage and reduce the discharging depth of the SMES. The single and comprehensive performances of the SAPF-based SMES in various scenarios have been attested through a series of comparisons based on a conventional SAPF and a SAPF-based battery energy storage (BES). The superiority and robustness of the proposed FLC method are identified through simulation comparisons with a classical proportional-integral controller and a sliding mode controller in various scenarios considered.

## 1. Introduction

Among various renewable energy sources (RESs), PV generation systems with merits of pollution-free, no geographical restrictions, and abundant reserves occupy an increasing proportion of the microgrid with extreme prospects [1,2]. With the improved penetration of the photovoltaic generation, the PV system is transferring from the past small-scale island mode to large-scale grid-connected mode [3]. Unfortunately, solar energy has strong randomness and obvious intermittentness, which leads to large power fluctuation in PV output [4-6]. Moreover, the microgrid contains a growing variety of loads, such as nonlinear, unbalanced, and pulsating loads, which inevitably produce harmonic, reactive, and unbalanced currents at the PCC and greatly imperil the grid stability [7-10].

As a traditional shunt active power filter (SAPF) is gradually unable to govern these issues, it is necessary to draw an updating method that can rapidly respond to the internal power quality problems of the PV microgrid. Considering that the energy storage device (ESD) with smoothing power fluctuation is an essential part for microgrid [11-14], the active filtering function can be integrated into the ESD to improve the utilization rate and to reduce the cost.

The widely-investigated ESDs can be classified into several categories: battery energy storage [15,16], supercapacitor energy storage [17], and superconducting magnetic energy storage (SMES) [18,19]. In [15] and [16], the SAPFs combined with battery energy storage and PV-battery are respectively presented to constrain harmonic current and mitigate transient oscillations caused by abrupt loads. However, the battery-based protection schemes are not suitable for applying in MW-class conditions. The service life of the battery will be seriously shortened on account of frequent power fluctuations. The supercapacitor-integrated SAPF is proposed in [17] to provide active and reactive power support for intermittent renewable energy. Although supercapacitor has the advantages of high-power density and fast response, the voltage sharing control for series capacitors is still an obstacle that needs to be addressed.

Unlike other energy storage technologies, the principle of SMES is to store energy in the form of a magnetic field, which is generated by DC current flowing through the SC [20]. Due to the zero-resistance characteristic of the superconductor, electrical energy can be stored in the SC with little loss. When electrical power is needed, the DC current stored in

* Corresponding author.
*E-mail address:* yqxing@hebut.edu.cn (Y.Q. Xing).

https://doi.org/10.1016/j.est.2021.102508
Received 8 January 2021; Received in revised form 17 March 2021; Accepted 18 March 2021
Available online 19 April 2021

**Table 1**
Comparison of VSC and CSC for SMES.

| Item | | VSC | CSC |
|---|---|---|---|
| Power regulation | | Good | Medium-good |
| Filtering performance | | Better | Good |
| Configuration | Grid-filter | *L*-filter | *C*-filter |
| | IGBTs | 8 | 6 |
| | Diodes | 2 | 6 |
| | Overvoltage protection circuit | No | Yes |
| | Cost | Medium-high | High |
| Efficiency | | Good | Medium-good |
| Total power losses | | Low | Lower |
| Complexity of control | | High | Medium-high |

the magnetic field of SC will be quickly injected into the grid with extreme high efficiency (over 90%) using power conditioning system (PCS). Therefore, the SMES is suitable for harmful currents compensation [18], dynamic voltage regulation [21], low voltage ride through and power fluctuation suppression [22,23], and alleviating sub-synchronous oscillation [24].

As an interface between SC and the grid, the PCS generally has two types of topologies: voltage source converter (VSC) with DC/DC converter [24] and current source converter (CSC) [25-26]. A series of comparisons between CSC and VSC with DC/DC converter in terms of performance, configuration, efficiency, and control complexity are shown in Table 1 [20,24,27]. Consequently, a VSC with DC/DC converter is employed to connected in parallel at the PCC in this paper.

Several control schemes have been proposed to preliminarily investigate the performance of the SMES integrated with SAPF [18,19]. In [18] and [19], the control techniques based on the modified synchronous reference frame and instantaneous symmetrical component theory are adopted to control the VSC to suppress the harmonic current and power fluctuation resulted from the pulsating load, respectively. However, the functions for mitigating unbalanced current and intermittent output of RESs have not been fully explored, resulting in a waste of equipment utilization.

On the other hand, the stable DC-link voltage is a vital prerequisite for the SMES to have excellent compensation capability. The hysteresis control method is adopted to regulate the DC-link voltage for reducing the capacitor ripple voltage in [18,19]. However, the operating frequency of the hysteresis controller is influenced by the fixed bandwidth, resulting in higher requirements for power switching devices. The performance of the SMES controlled by the proportional-integral (PI) method in [21-22] is easily affected by the controller parameters. Moreover, a fuzzy logic controller is proposed to mitigate power

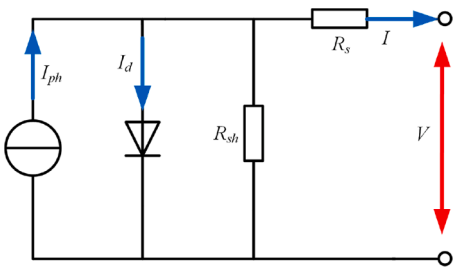


**Fig. 2.** The equivalent circuit diagram of the PV cell.

fluctuation in [28-31]. However, the DC-link voltage error is not used as the input of the fuzzy logic controller, but as the input of the outer loop PI regulator of the AC side converter, resulting in larger voltage oscillation when power fluctuation occurs.

To reduce the capital cost and simultaneously improve the utilization rate of the SMES, the multi-objective control technique and fuzzy logic control method are proposed to achieve the dual functions of active filtering and power fluctuation suppression for the SAPF-based SMES. To follow up our previous study [32], i.e., a new step-shape solenoidal SC is proposed to enhance the critical current and energy storage capacity under the determined amount of superconducting tape, a sample step-shape SC is employed for the method verification.

Compared with other combination solutions, this work extends the earlier research and application of the SAPF-based SMES as follows:

1) The SAPF-based SMES provides an integrated protection for harmful currents and power fluctuations in PV microgrid.
2) The modified $i_p - i_q$ method is proposed to extract reference current.
3) The fuzzy logic control method is designed to maintain the DC-link voltage stability and reduce depth of discharge of the SMES.

The remainder of this paper is organized as follows. Section 2 introduces the modeling of PV microgrids equipped with the SAPF-based SMES. Section 3 presents the control schemes of the entire system. Simulation results are presented and analyzed in Section 4. Conclusions are drawn from this work in Section 5.

## 2. Modeling of PV microgrid

As shown in Fig. 1, the PV microgrid model consists of three parts: i) PV grid-connected system; ii) Four different types of loads (three-phase balanced load $\boldsymbol{L}_1$, nonlinear load $\boldsymbol{L}_2$, unbalanced load $\boldsymbol{L}_3$, and pulsating load $\boldsymbol{L}_4$); iii) SAPF-based SMES.

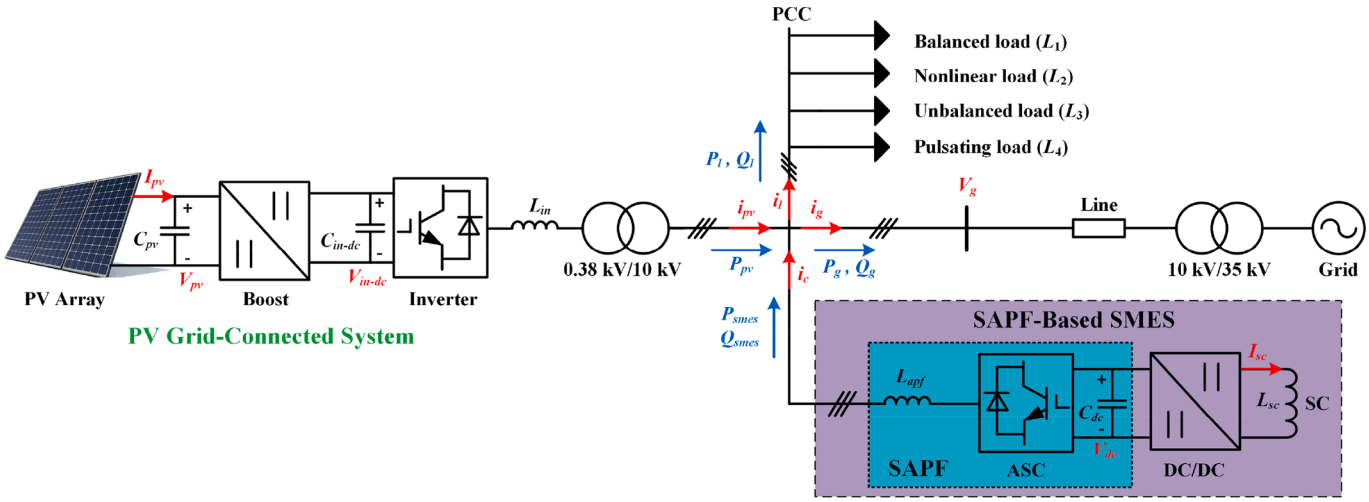


**Fig. 1.** Structure of the SAPF-Based SMES for PV microgrid.

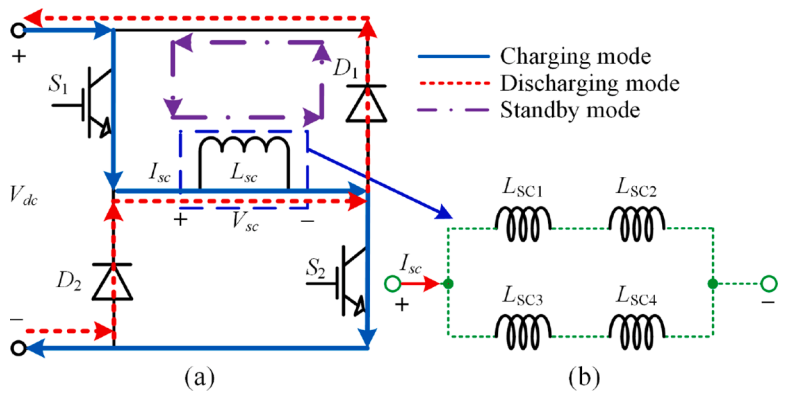


**Fig. 3.** The structure of the SMES. (a) Topology of DC/DC converter integrated with SC; (b) The electrical connection of the SC employed.

### 2.1. PV Grid-Connected System

1) PV Array: The equivalent circuit diagram of the PV cell is shown in Fig. 2. The generated photocurrent $I_{ph}$ can be considered approximately equal to the short-circuit current $I_{sc}$ when the current $I_d$ flowing through the diode is negligible. A PV array is made up of hundreds of PV cells in series and parallel. The relationship between PV array output voltage $V_{pv}$ and current $I_{pv}$ can be expressed as follows [33]:

$$I_{pv} = N_p I_{sc} - N_p I_0 \left\{ \exp\left[ \frac{q\left(V_{pv} + I_{pv}\left(N_s/N_p\right)R_s\right)}{N_s AkT} \right] - 1 \right\} \tag{1}$$

where $I_0$ is diode reverse saturation current; $R_s$ is PV cell equivalent series resistance; $q$ is the electronic charge ($1.602 \times 10^{-19}$ C); $k$ is Boltzmann constant ($1.38 \times 10^{-23}$ J/K); $N_s$ and $N_p$ are the number of PV cells in series and parallel, respectively; $T$ and $A$ are temperature and the curve-fitting factor of the PV cell, respectively. The selected temperature value is 25 °C in this paper.

2) DC/DC Boost Converter: A DC-DC boost converter is employed to implement the maximum power point tracking (MPPT) control of the PV array in the Fig. 1.

3) PV Inverter: The PV inverter is a voltage source converter (VSC) connected to the PCC via an $L$-filter and a 0.38 kV/10 kV transformer. Assuming that all the related vectors are transformed into the $d$-$q$ reference frame, the mathematical model of PV inverter can be obtained as follows [34]:

$$\begin{cases} V_{ind} = L_{in}\dfrac{dI_{ind}}{dt} + R_{in}I_{ind} - \omega L_{in}I_{inq} + V_d \\ V_{inq} = L_{in}\dfrac{dI_{inq}}{dt} + R_{in}I_{inq} + \omega L_{in}I_{ind} + V_q \end{cases} \tag{2}$$

where $V_{ind}$, $V_{inq}$ and $I_{ind}$, $I_{inq}$ are the $d$-axis and $q$-axis components of PV inverter output terminal, respectively; $\omega$ is rotation angle frequency; $L_{in}$ and $R_{in}$ represent filter inductance and resistance, respectively.

**Table 2**
Analysis of the SMES operation mode.

| DC-link voltage error $\Delta V_{dc}$ | Duty cycle $D$ | Operation mode |
|---|---|---|
| $\Delta V_{dc} < 0$ | $D > 0.5$ | Charging mode |
| $\Delta V_{dc} > 0$ | $D < 0.5$ | Discharging mode |
| $\Delta V_{dc} = 0$ | $D = 0.5$ | Standby mode |

### 2.2. SAPF-Based SMES

As an inductive energy storage device, the real-time residual energy $E_{smes}$ during the SMES operation can be estimated as [35]:

$$E_{smes} = \frac{1}{2}L_{sc}I_{sc}^2 \tag{3}$$

where $L_{sc}$ and $I_{sc}$ are inductance and current of the SC.

Structurally, the SAPF-based SMES shown in the Fig. 1 can be regarded as composed of a SAPF and a DC/DC converter integrated with SC, connected in parallel to the DC-link capacitor terminal.

1) SAPF: The SAPF is a converter interfaced to the PCC for suppressing harmonic, reactive, and unbalanced currents. The other two essential components are the supporting capacitor $C_{dc}$ for the DC-link and the $L$-filter $L_{apf}$ for the AC side, respectively. The working principle of SAPF can be described as:

$$\boldsymbol{i}_c = \boldsymbol{i}_{hl} + \boldsymbol{i}_{ul} \tag{4}$$

where $\boldsymbol{i}_c$ is the SAPF output compensation current; $\boldsymbol{i}_{hl}$ and $\boldsymbol{i}_{ul}$ are the harmonic and unbalanced currents, respectively.

In addition to the active filtering function, the SAPF-based SMES also has the function of mitigating power fluctuations. The relationship among output current $\boldsymbol{i}$, active power $P$, and reactive power $Q$ of grid side, PV generation side, SMES side, and load side is as follows:

$$\begin{cases} \boldsymbol{i}_g = \boldsymbol{i}_{pv} + \boldsymbol{i}_c - \boldsymbol{i}_l \\ P_g = P_{pv} + P_{smes} - P_l \\ Q_g = Q_{smes} - Q_l \end{cases} \tag{5}$$

where subscripts $g$, $pv$, $smes$, and $l$ represent the grid side, PV inverter, SMES side, and load side variables, respectively.

2) DC/DC Converter: The DC/DC converter is an interface for coupling the SC with the DC-link of SAPF, as illustrated in Fig. 3(a). Although the current direction through the SC is consistent in different operating modes, the voltage polarity of the SC terminal is different. The relationship between the average voltage $V_{sca}$ of the SC terminal and DC-link voltage $V_{dc}$ in a cycle is as follows [36]:

$$V_{sca} = (2D - 1)V_{dc} \tag{6}$$

where $D$ is the duty cycle of the two insulated gate bipolar transistors (IGBTs) $S_1$ and $S_2$.

According to (6), the duty cycle $D$ determines the operation mode of

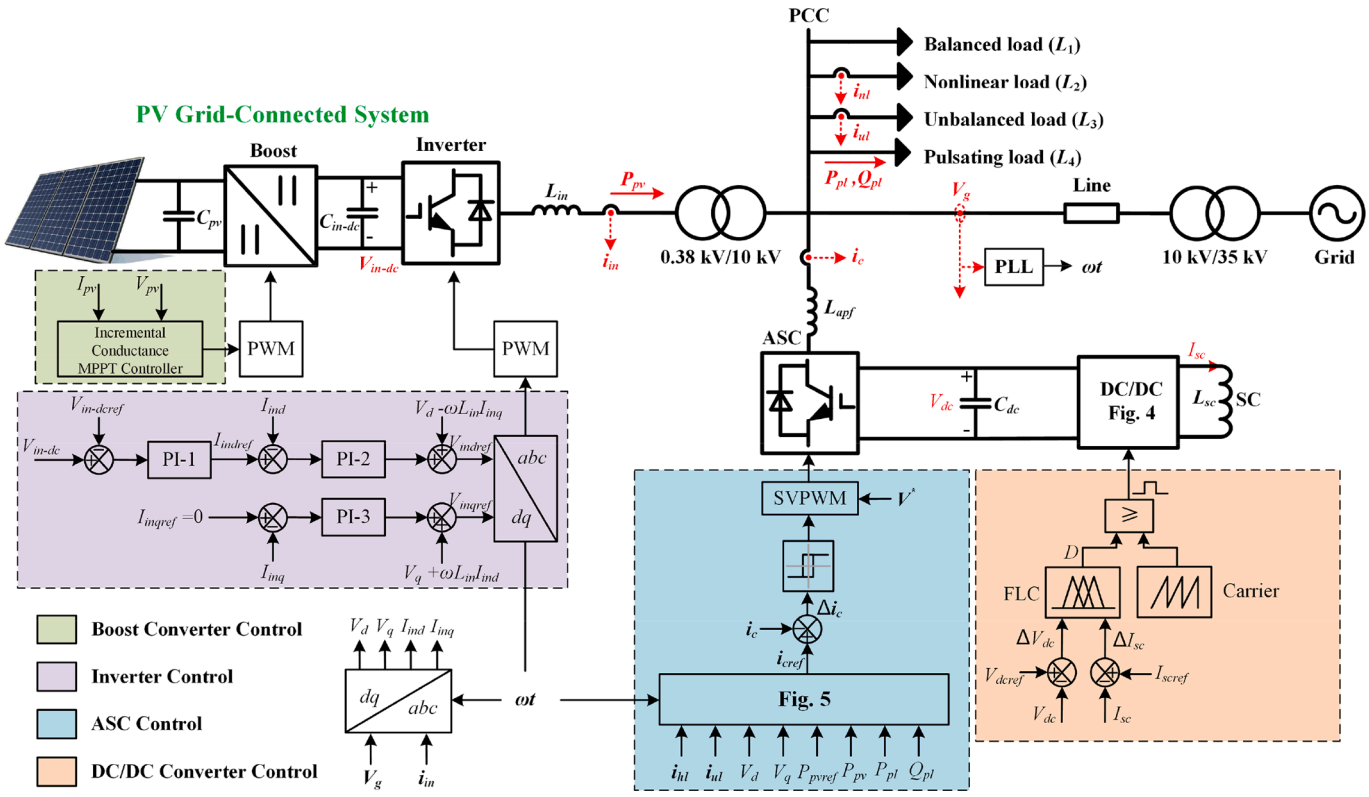


**Fig. 4.** Control schematic diagram of the entire system.

SMES. When the DC-link voltage error $\Delta V_{dc}$ is less than zero, the SMES needs to absorb the surplus energy for stabilizing the DC-link voltage, and vice versa. Therefore, the relationship among $\Delta V_{dc}$, $D$, and the SMES operating mode is shown in Table 2.

3) Superconducting coil: In order to lower the capital cost of the SAPF-based SMES, a 1.193 H/ 1760 A SC employed in this paper is formed by four 1.193 H/ 880 A step-shaped solenoidal coil units (SC1, SC2, SC3, and SC4) [32], as shown in Fig. 3(b). The superconducting tape selected is Dynamically Innovative BSCCO (DI-BSCCO) tapes [37] with a total length of 20872 m. In comparison, the tape usage of the step-shaped SC is 0.8 times than that of the traditional rectangular-shaped SC, and the critical current is 1.4 times than that of the conventional rectangular-shaped SC, which indicates that the step-shaped SC is more cost-effective in energy storage.

The cost of a SMES unit mainly depends on its capacity and consequently the amount of the superconductor used. Along with the development and maturation of superconducting technology, a practical SMES becomes feasible. Moreover, compared with conventional SAPF, the application of SAPF-based SMES is to provide an integrated protection for harmful currents and power fluctuations in PV microgrid, which leads to a further cost reduction of the SMES.

## 3. Control schemes for the entire system

According to the overall layout of the entire system depicted in the Fig. 1, four types of converters are employed, i.e., DC/DC boost converter, PV inverter, ASC (the SMES AC side converter), and DC/DC converter. The control schemes of each converter are shown in Fig. 4.

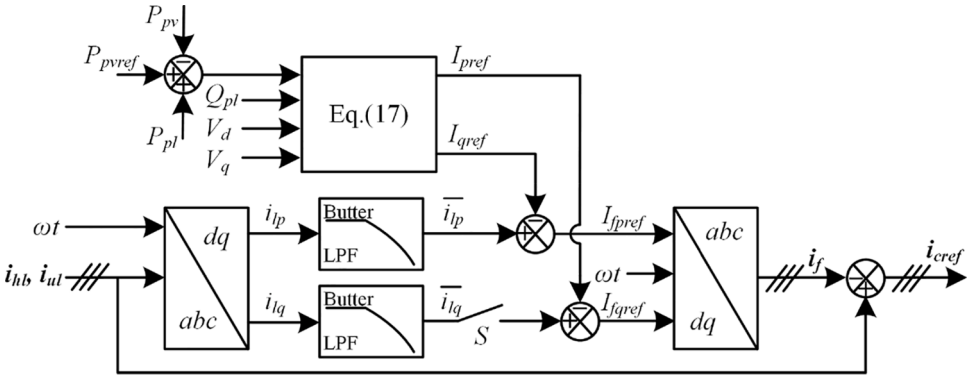


**Fig. 5.** Schematic diagram of the modified $i_p - i_q$ method.

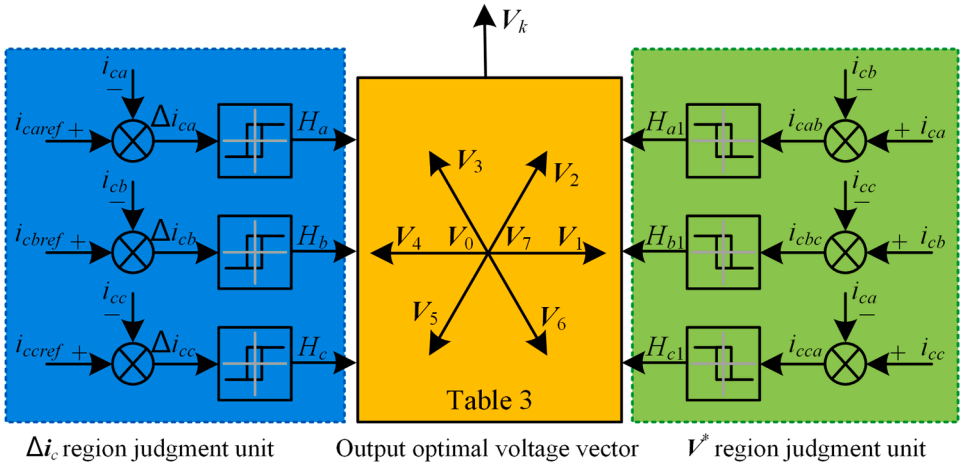


**Fig. 6.** Schematic diagram of hysteresis SVPWM method.

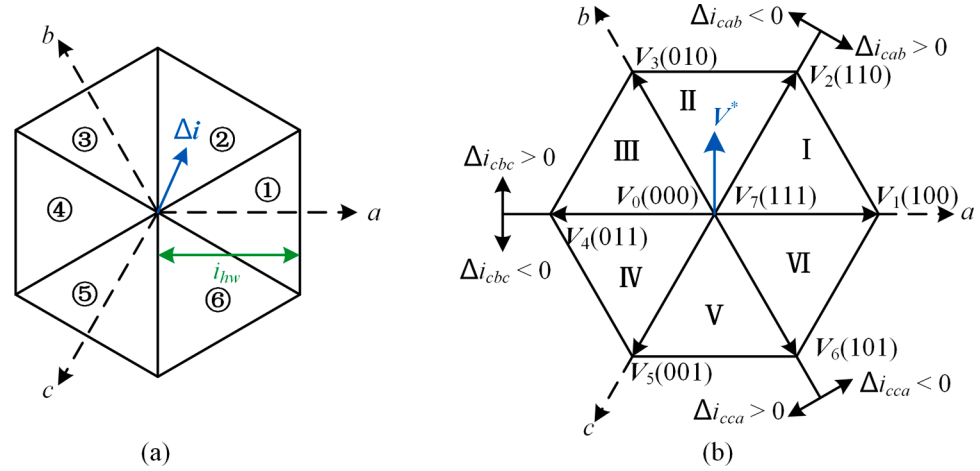


**Fig. 7.** The region divisions of $\Delta i$ and $V^*$.

**Table 3**
Optimal output voltage vector.

| Region of $V^*$ ($\Delta i_{cab}$, $\Delta i_{cbc}$, $\Delta i_{cca}$) | Region of $\Delta i$ | | | | | |
|---|---|---|---|---|---|---|
| | ① | ② | ③ | ④ | ⑤ | ⑥ |
| I (+ + −) | $V_1$ | $V_2$ | $V_2$ | $V_{0,7}$ | $V_{0,7}$ | $V_1$ |
| II (− + −) | $V_2$ | $V_2$ | $V_3$ | $V_3$ | $V_{0,7}$ | $V_{0,7}$ |
| III (− + +) | $V_{0,7}$ | $V_3$ | $V_3$ | $V_4$ | $V_4$ | $V_{0,7}$ |
| VI (− − +) | $V_{0,7}$ | $V_{0,7}$ | $V_4$ | $V_4$ | $V_5$ | $V_5$ |
| V (+ − +) | $V_6$ | $V_{0,7}$ | $V_{0,7}$ | $V_5$ | $V_5$ | $V_6$ |
| IV (+ − −) | $V_1$ | $V_1$ | $V_{0,7}$ | $V_{0,7}$ | $V_6$ | $V_6$ |

### 3.1. Control of PV generation system

1) DC/DC Boost Converter Control: The DC/DC boost converter is adopted to track the maximum power point of the PV array using the incremental conductance method [38].
2) PV Inverter Control: Voltage and current dual-loop control method is adopted to control the PV inverter for outputting the active power $P_{pv}$ generated by PV array. The control target of the voltage outer loop PI regulator is to stabilize the DC-link voltage of the PV inverter. The outer loop PI-1 regulator input is the DC-link voltage error $\Delta V_{in-dc}$ and the output $I_{indref}$ is used as the reference current of the inner loop PI-2 regulator. Since PV grid-connected system needs to operate under unity power factor condition, the reference current $I_{inqref}$ of the inner loop PI-3 regulator is zero. The mathematical expression is as follows:

$$\begin{cases} I_{indref} = \left(K_{op} + \dfrac{1}{K_{oi}s}\right)\left(V_{in-dc} - V_{in-dcref}\right) \\ I_{inqref} = 0 \end{cases} \tag{7}$$

where $V_{in-dc}$ and $V_{in-dcref}$ are the DC-link actual and reference voltages, respectively; $K_{op}$ and $K_{oi}$ are the proportional and integral parameters of the PI-1 regulator, respectively.

It can be seen from (2) that PV output current components $I_{ind}$ and $I_{inq}$ are coupled with each other. Therefore, the feedforward decoupling method is utilized to control the inner loop current. The reference voltage $V_{indref}$ and $V_{inqref}$ can be obtained as follows:

$$\begin{cases} V_{indref} = \left(K_{ip} + \dfrac{1}{K_{ii}s}\right)\left(I_{indref} - I_{ind}\right) - \omega L_{in} I_{inq} + V_d \\ V_{inqref} = \left(K_{ip} + \dfrac{1}{K_{ii}s}\right)\left(I_{inqref} - I_{inq}\right) + \omega L_{in} I_{ind} + V_q \end{cases} \tag{8}$$

where $K_{ip}$ and $K_{ii}$ are the proportional and integral parameters of PI-2 and PI-3 regulators, respectively.

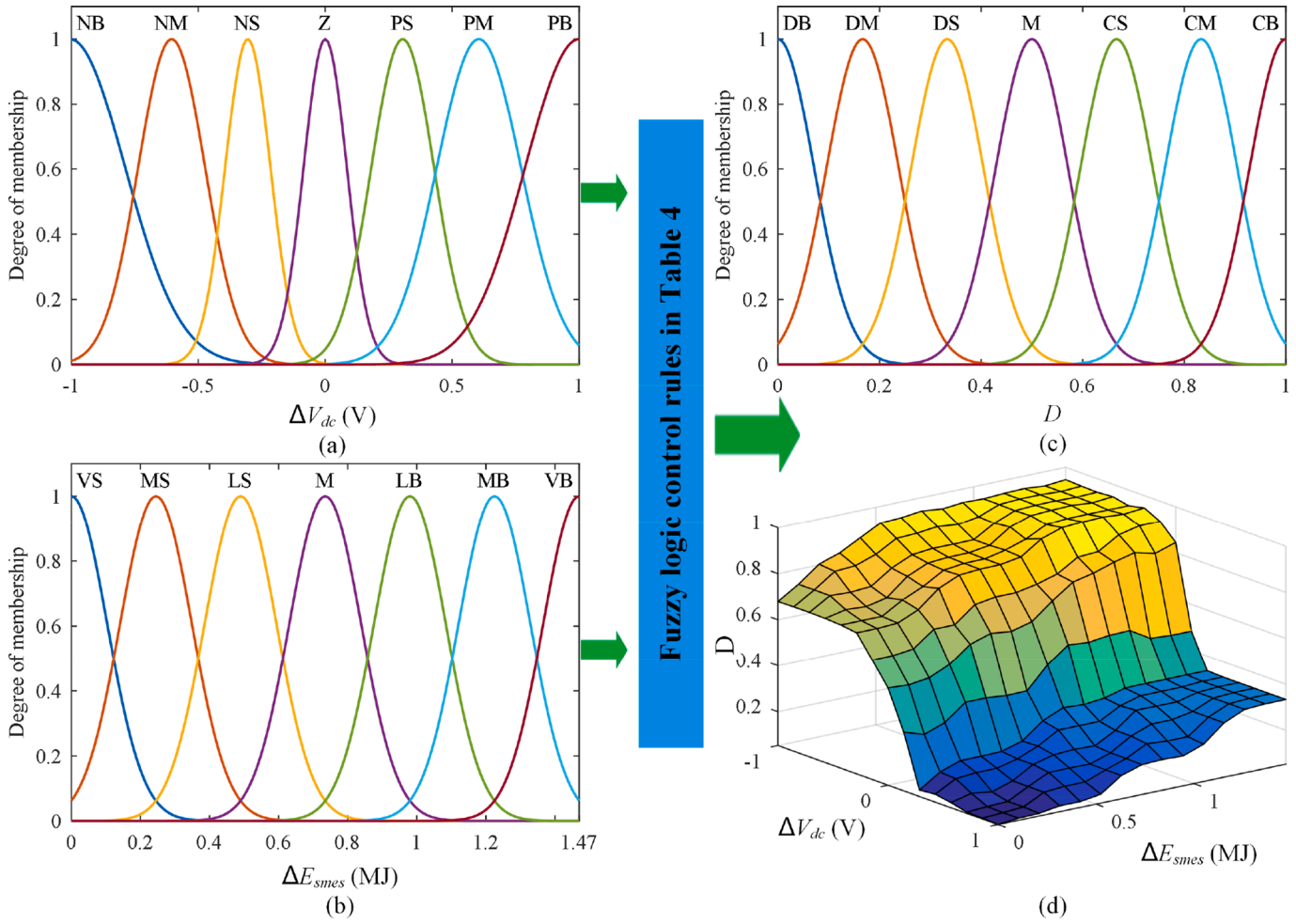


**Fig. 8.** Principle of the proposed FLC method. (a) MFs of the first input $\Delta V_{dc}$; (b) MFs of the second input $\Delta E_{smes}$; (c) MFs of output $D$; (d) 3-D graph for DISO FLC MFs.

**Table 4**
Fuzzy logic control rules.

| $D$ | | $\Delta E_{smes}$ | | | | | | |
|---|---|---|---|---|---|---|---|---|
| | | VS | MS | LS | M | LB | MB | VB |
| $\Delta V_{dc}$ | NB | CS | CM | CB | CB | CB | CB | CB |
| | NM | CS | CM | CM | CB | CB | CB | CB |
| | NS | CS | CS | CM | CM | CB | CB | CB |
| | Z | M | M | CS | CS | CM | CB | CB |
| | PS | DB | DM | DM | DS | DS | DS | DS |
| | PM | DB | DB | DM | DM | DS | DS | DS |
| | PB | DB | DB | DB | DM | DM | DS | DS |

### 3.2. Control of the SAPF-based SMES

#### 3.2.1. ASC Control

In the proposed multi-objective control technique, the ASC of the SAPF-Based SMES aims to compensate for the harmonic, reactive, and negative sequence components existing in grid-connected current and mitigating power fluctuations resulted from the pulsating load and the intermittent renewable energy. The control technique consists of two parts: i) Extraction of reference current; ii) Generation of required compensation current.

*3.2.1.1. Extraction of reference current.* The modified $i_p - i_q$ method combining instantaneous reactive power theory [39] and power decoupling control [34] is proposed to detect and calculate the reference current, as illustrated in Fig. 5.

1) According to the symmetric component method, the nonlinear current $i_{hl}$ and unbalanced current $i_{ul}$ can be decomposed into:

$$\begin{bmatrix} i_{hla} \\ i_{hlb} \\ i_{hlc} \end{bmatrix} = \sum_{k=0}^{\infty} \begin{bmatrix} I_{hl(2k+1)}\sin((2k+1)\omega t + \theta_{2k+1}) \\ I_{hl(2k+1)}\sin\left((2k+1)\left(\omega t - \frac{2\pi}{3}\right) + \theta_{2k+1}\right) \\ I_{hl(2k+1)}\sin\left((2k+1)\left(\omega t + \frac{2\pi}{3}\right) + \theta_{2k+1}\right) \end{bmatrix} \tag{9}$$

$$\begin{bmatrix} i_{ula} \\ i_{ulb} \\ i_{ulc} \end{bmatrix} = \begin{bmatrix} I_{ulps}\sin(\omega t + \theta_{ps}) \\ I_{ulps}\sin\left(\omega t + \theta_{ps} - \frac{2\pi}{3}\right) \\ I_{ulps}\sin\left(\omega t + \theta_{ps} + \frac{2\pi}{3}\right) \end{bmatrix} + \begin{bmatrix} I_{ulns}\sin(\omega t + \theta_{ns}) \\ I_{ulns}\sin\left(\omega t + \theta_{ns} + \frac{2\pi}{3}\right) \\ I_{ulns}\sin\left(\omega t + \theta_{ns} - \frac{2\pi}{3}\right) \end{bmatrix} + \begin{bmatrix} I_{ul0}\sin(\omega t + \theta_0) \\ I_{ul0}\sin(\omega t + \theta_0) \\ I_{ul0}\sin(\omega t + \theta_0) \end{bmatrix} \tag{10}$$

where $I$, and $\theta$ is amplitude and initial phase angle, respectively; subscript $k$ represents the harmonic order, and $k = 1$ & $k > 1$ represent the fundamental and harmonic components, respectively; subscripts *ps*, *ns*, and 0 represent positive sequence, negative sequence, and zero sequence components, respectively; $\omega t$ is the transformation angle obtained through the phase-locked loop (PLL).

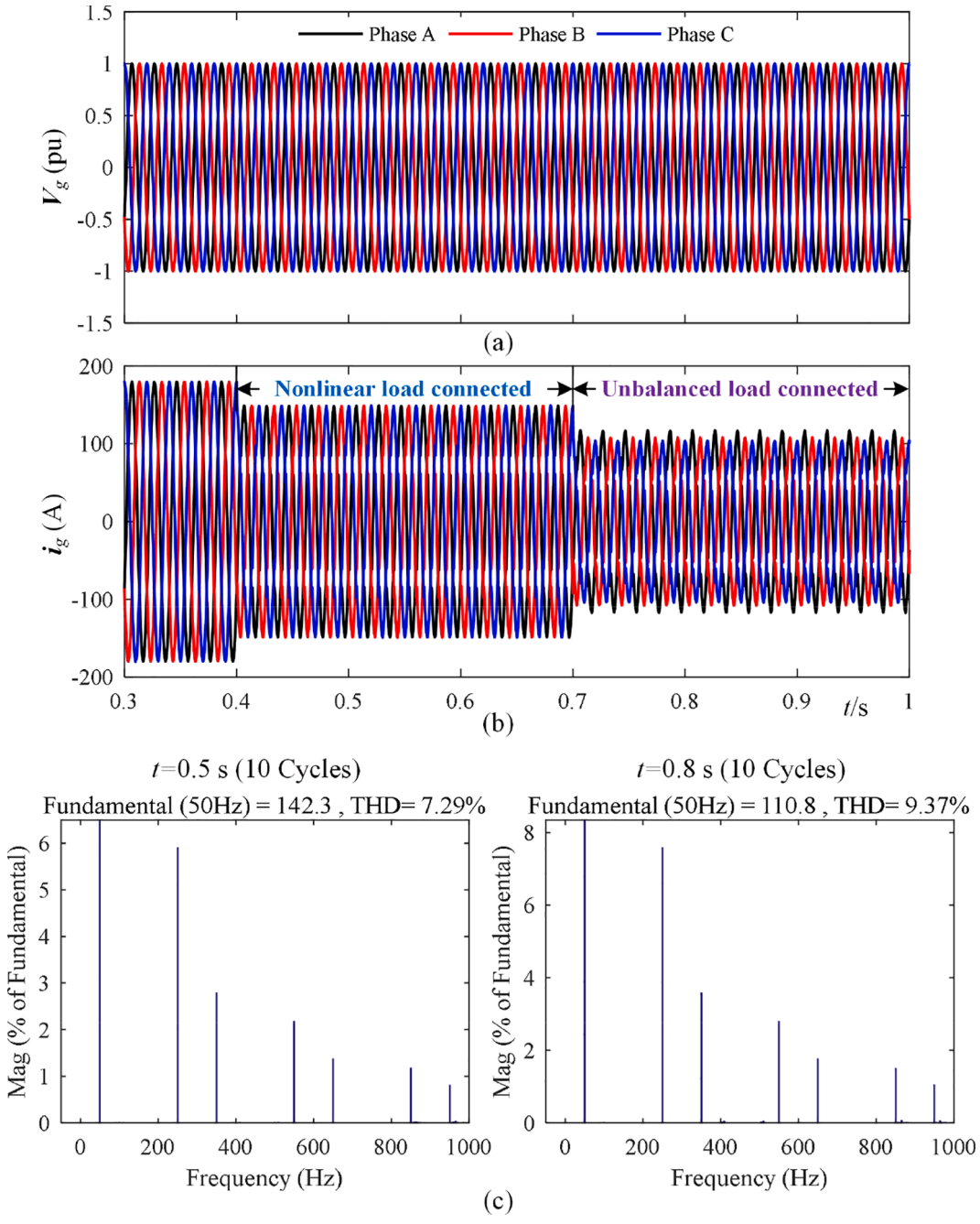


**Fig. 9.** Profiles of grid side voltage and current with no compensator and harmonic spectrum of current at $t$=0.5 s and 0.8 s.

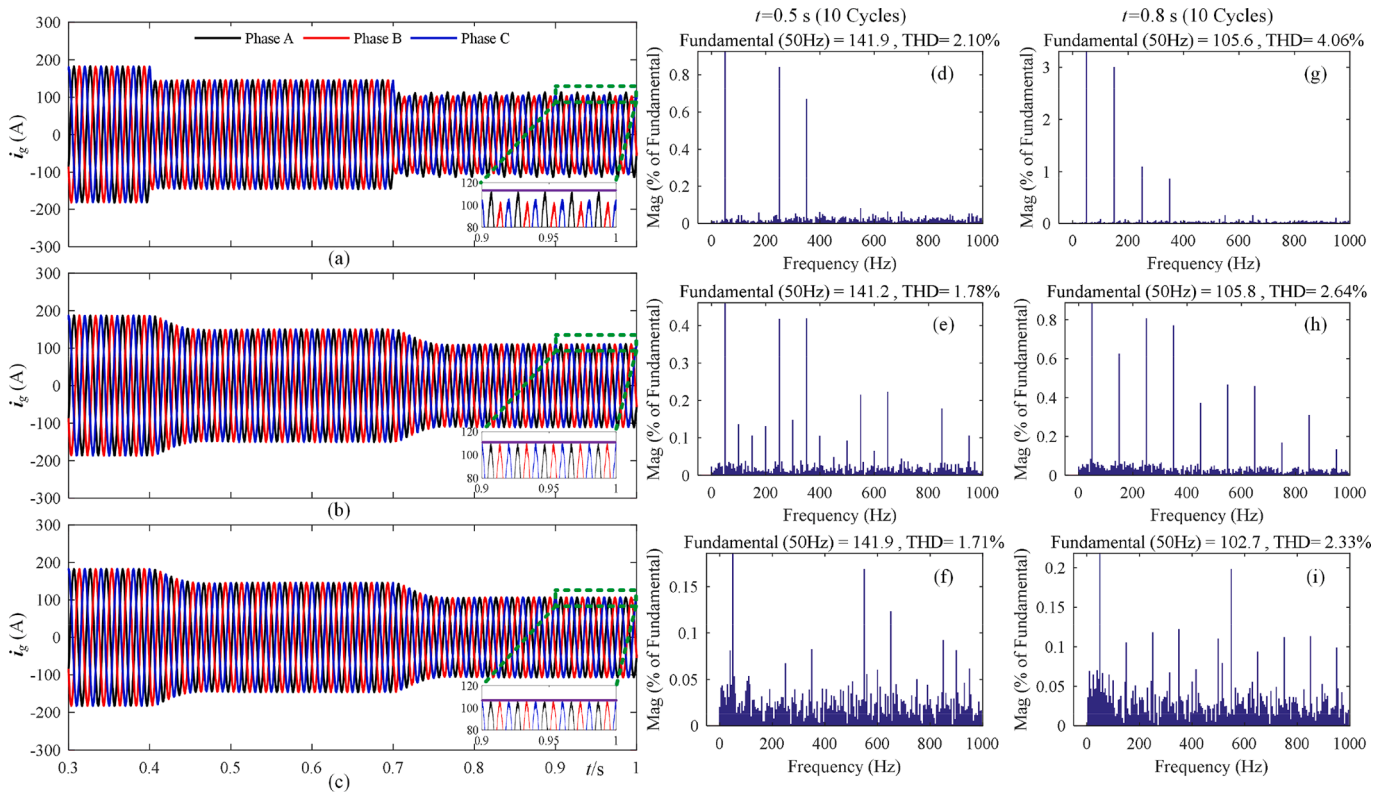


**Fig. 10.** Responses and harmonic spectrum of grid side current with the three types of protection device. (a) With SAPF; (b) With SAPF-based BES; (c) With SAPF-based SMES; (d ~ f) Harmonic spectrum at $t$=0.5 s; (g ~ i) Harmonic spectrum at $t$=0.8 s.

Since there is no zero-sequence current in the three-phase three-wire system, according to (11) [40], the forms of (9) and (10) can be derived as follows:

$$T=\frac{2}{3}\begin{bmatrix}\cos\omega t & \cos\left(\omega t-\frac{2\pi}{3}\right) & \cos\left(\omega t+\frac{2\pi}{3}\right)\\ -\sin\omega t & -\sin\left(\omega t-\frac{2\pi}{3}\right) & -\sin\left(\omega t+\frac{2\pi}{3}\right)\end{bmatrix} \tag{11}$$

$$\begin{bmatrix}i_{hlp}\\ i_{hlq}\end{bmatrix}=\begin{bmatrix}I_{hl1}\sin\theta_1\\ -I_{hl1}\cos\theta_1\end{bmatrix}+\begin{bmatrix}\sum_{n=7,13\ldots}^{\infty}I_{hln}[\sin(n-1)\omega t+\theta_n]\\ \sum_{n=7,13\ldots}^{\infty}I_{hln}[\cos(n-1)\omega t+\theta_n]\end{bmatrix}+\begin{bmatrix}\sum_{n=5,11\ldots}^{\infty}I_{hln}[\sin(n+1)\omega t+\theta_n]\\ \sum_{n=5,11\ldots}^{\infty}I_{hln}[\cos(n+1)\omega t+\theta_n]\end{bmatrix} \tag{12}$$

$$\begin{bmatrix}i_{ulp}\\ i_{ulq}\end{bmatrix}=\begin{bmatrix}I_{ulps}\sin\theta_{ps}+I_{ulns}\sin(2\omega t+\theta_{ns})\\ -I_{ulps}\cos\theta_{ps}+I_{ulns}\cos(2\omega t+\theta_{ns})\end{bmatrix} \tag{13}$$

Combining (12) and (13), it can be obtained:

$$\begin{bmatrix}i_{lp}\\ i_{lq}\end{bmatrix}=\begin{bmatrix}i_{hlp}+i_{ulp}\\ i_{hlq}+i_{ulq}\end{bmatrix} \tag{14}$$

$$\begin{bmatrix}\overline{i_{lp}}\\ \overline{i_{lq}}\end{bmatrix}=\begin{bmatrix}I_{hl1}\sin\theta_1+I_{ulps}\sin\theta_{ps}\\ -I_{hl1}\cos\theta_1-I_{ulps}\cos\theta_{ps}\end{bmatrix} \tag{15}$$

where subscripts $p$ and $q$ represent instantaneous active and reactive components, respectively.

It can be seen from (12) and (13) that the harmonic and negative sequence components appear in the $d$ and $q$ channels with six times and double frequency, respectively. Only the fundamental positive sequence active and reactive components of the nonlinear and balanced currents are DC components. Therefore, the DC components $\overline{i_{lp}}$ and $\overline{i_{lq}}$ can be obtained using the second-order Butterworth low-pass filter (LPF), as shown in (15). Besides, assuming that switch $S$ shown in the Fig. 5 is off, i.e., $\overline{i_{lq}}=0$, complete reactive power compensation can be implemented.

2) Considering that the power fluctuations of PV microgrid are resulted from variable solar irradiance and the pulsating load in this paper, the reference active and reactive power demands $P_{ref}$ and $Q_{ref}$ can be obtained as follows:

$$\begin{cases}P_{ref}=P_{pvref}-P_{pv}+P_{pl}\\ Q_{ref}=Q_{pl}\end{cases} \tag{16}$$

where $P_{pvref}$ and $P_{pv}$ are the rated and actual PV output active power, respectively; $P_{pl}$ and $Q_{pl}$ are the active and reactive power of pulsating load, respectively.

To simplify the calculation process, it is assumed that the grid voltage $V_g$ is oriented in the $d$-axis, i.e., $V_d=V_g$, $V_q=0$. According to the relationship between the SMES output power and grid voltage, the power reference current $I_{pref}$, $I_{qref}$ can be calculated as follows:

$$\begin{cases}I_{pref}=\dfrac{2P_{ref}}{3V_d}\\ I_{qref}=-\dfrac{2Q_{ref}}{3V_d}\end{cases} \tag{17}$$

According to (15) and (17), the synthetic reference current command of the two parts is given by:

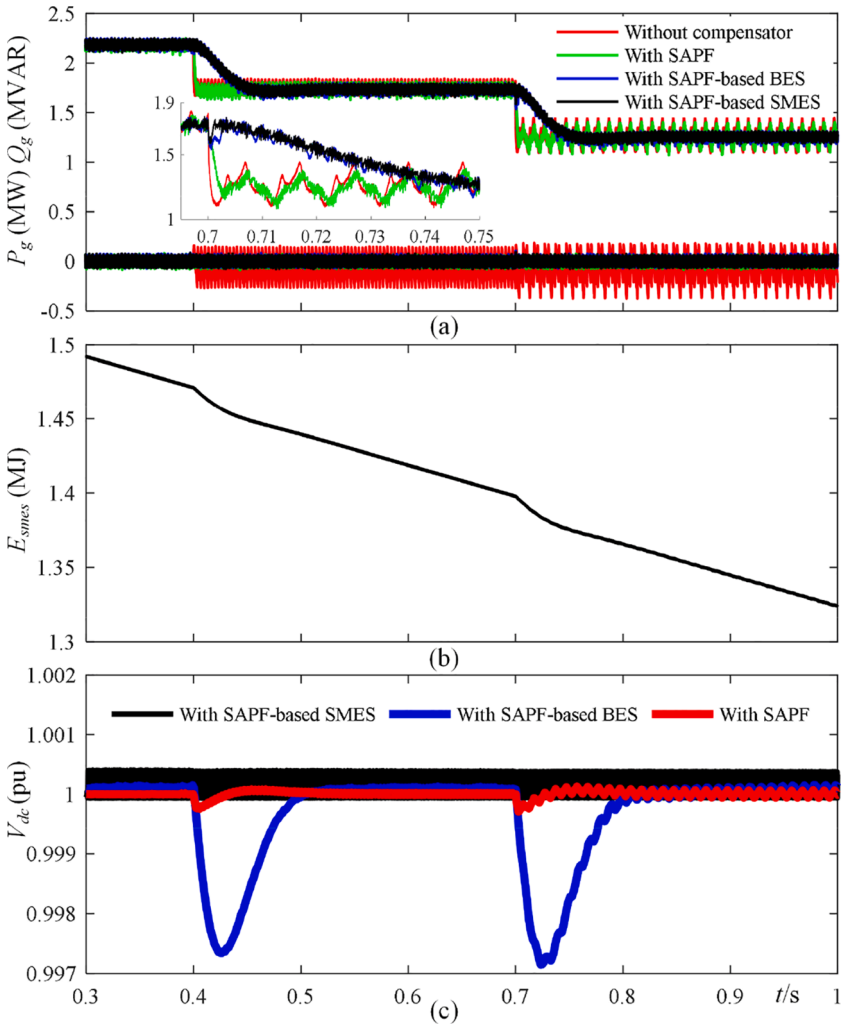


**Fig. 11.** Comparisons among SAPF, SAPF-based BES and SAPF-based SMES in scenario 1. (a) Grid side active and reactive power; (b) Residual energy storage of SMES; (c) DC-link voltage.

$$\begin{cases} I_{fpref} = \overline{i_{lp}} - I_{pref} \\ I_{fqref} = -I_{qref} \end{cases} \tag{18}$$

where subscript $f$ represents the fundamental component.

3) After the synthetic reference current of the ASC is obtained, the fundamental positive sequence components in the $d$-$q$ reference frame are transformed to the stationary $abc$ reference frame. By subtracting the fundamental positive sequence current $\boldsymbol{i}_f$ from the sampling total load current $\boldsymbol{i}_l$, the comprehensive compensation current $\boldsymbol{i}_{cref}$ can be given as follows:

$$\boldsymbol{i}_{cref} = \boldsymbol{i}_l - \boldsymbol{i}_f \tag{19}$$

*3.2.1.2. Generation of Compensation Current.* Hysteresis SVPWM method is utilized to track the reference current for generating the required compensation current [41], as shown in Fig. 6. The ASC output voltage vector $\boldsymbol{V}_k$ mainly depends on the vector space regions where the error current vector $\Delta\boldsymbol{i}$ and the reference voltage vector $\boldsymbol{V}^*$ are located. The region divisions of $\Delta\boldsymbol{i}$ and $\boldsymbol{V}^*$ are shown in Figs. 7(a) and (b). On the one hand, the error currents ($\Delta i_{ca}$, $\Delta i_{cb}$, $\Delta i_{cc}$) are used as the input of the hysteresis controllers, and the output state values ($H_a$, $H_b$, $H_c$) determine its region. On the other hand, the region of $\boldsymbol{V}^*$ is determined by the polarities of the line current errors ($\Delta i_{cab}$, $\Delta i_{cbc}$, $\Delta i_{cca}$). Once the two regions are determined, the corresponding $\boldsymbol{V}_k$ can be selected according to Table 3.

$$\begin{bmatrix} \Delta i_{ca} \\ \Delta i_{cb} \\ \Delta i_{cc} \end{bmatrix} = \begin{bmatrix} i_{caref} - i_{ca} \\ i_{cbref} - i_{cb} \\ i_{ccref} - i_{cc} \end{bmatrix} \tag{20}$$

$$\begin{bmatrix} \Delta i_{cab} \\ \Delta i_{cbc} \\ \Delta i_{cca} \end{bmatrix} = \begin{bmatrix} i_{ca} - i_{cb} \\ i_{cb} - i_{cc} \\ i_{cc} - i_{ca} \end{bmatrix} \tag{21}$$

*3.2.2. DC/DC Converter Control*

For the DC/DC converter, the dual input and single output (DISO) fuzzy logic controller is employed to control the DC-link voltage stability and optimize the charging and discharging performance of the SMES. The principle of the proposed FLC method is illustrated in Fig. 8.

The first input of the FLC is the voltage error ($\Delta V_{dc}$), which indicates the difference between the DC-link voltage reference and actual value for judging the operating mode of the SMES, as shown in Table 2. The second input is the difference between the initial energy and the real-time residual energy of SMES ($\Delta E_{smes}$) for mitigating discharging deep. The output of the FLC is the duty cycle ($D$), which is compared with a 10 kHz sawtooth carrier for generating the PWM required by the two IGBTs. The domains of $\Delta V_{dc}$, $\Delta E_{smes}$ and $D$ are [-1, 1], [0, 1.47], and [0, 1], respectively. They are respectively defined as seven fuzzy subsets, as follows:

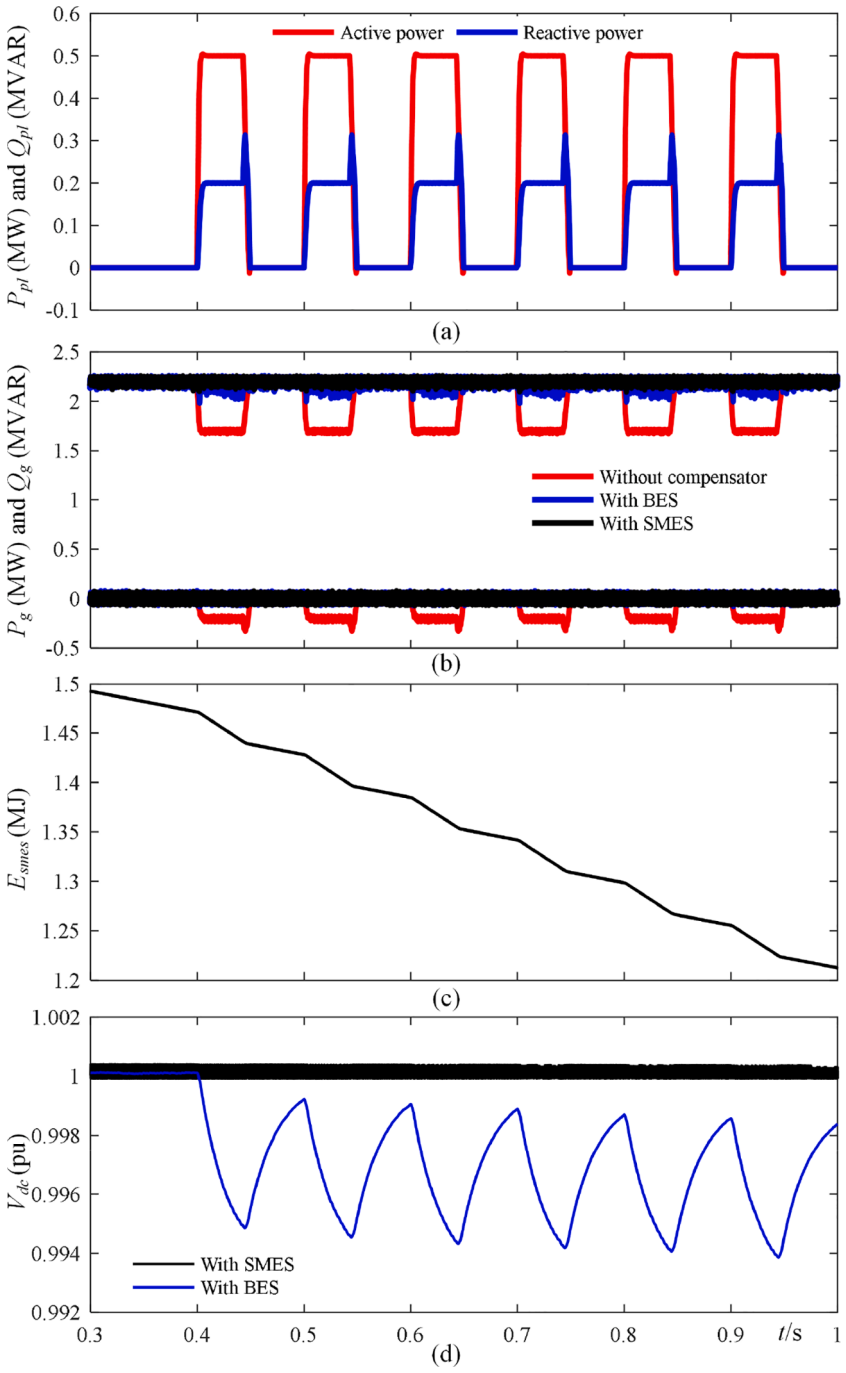


**Fig. 12.** Comparisons between BES and SMES in scenario 2. (a) Pulsating load power fluctuation; (b) Grid side active and reactive power; (c) Residual energy storage of SMES; (d) DC-link voltage.

$$\begin{cases} \Delta V_{dc} = \{\text{NB}, \text{NM}, \text{NS}, \text{Z}, \text{PS}, \text{PM}, \text{PB}\} \\ \Delta E_{smes} = \{\text{VS}, \text{MS}, \text{LS}, \text{M}, \text{LB}, \text{MB}, \text{VB}\} \\ D = \{\text{DB}, \text{DM}, \text{DS}, \text{M}, \text{CS}, \text{CM}, \text{CB}\} \end{cases} \tag{22}$$

where NB, NM, NS, Z, PS, PM, and PB are indicated as negative large, negative medium, negative small, zero, positive small, positive middle, and positive big, respectively; VS, MS, LS, M, LB, MB, and VB are indicated as very small, medium small, little small, medium, little big, medium big, and very big, respectively; DB, DM, DS, M, CS, CM, and CB are indicated as discharge big, discharge medium, discharge small, medium, charge small, charge medium, and charge big, respectively.

As shown in the Fig. 8, Gaussian membership functions (MFs) are adopted to improve the performance of the designed FLC controller. The setting rules of the membership function for the first input $\Delta V_{dc}$ follow: Near the zero point, the curve is steep; Far away from the zero point, the curve is gentle. Moreover, the format of "IF A AND B, THEN C" is adopted to establish the fuzzy logic control rules, as depicted in Table 4.

## 4. Simulation results and analysis

A 3 MW PV microgrid connected with SAPF-based SMES shown in the Fig. 1 is modeled using MATLAB/SIMULINK. The simulation parameters of PV grid-connected system, SAPF-based SMES, and various loads are designed as shown in Table A1 ~ A3.

In this section, a conventional SAPF and a SAPF-based BES will be simulated to compare with the SAPF-based SMES for single and

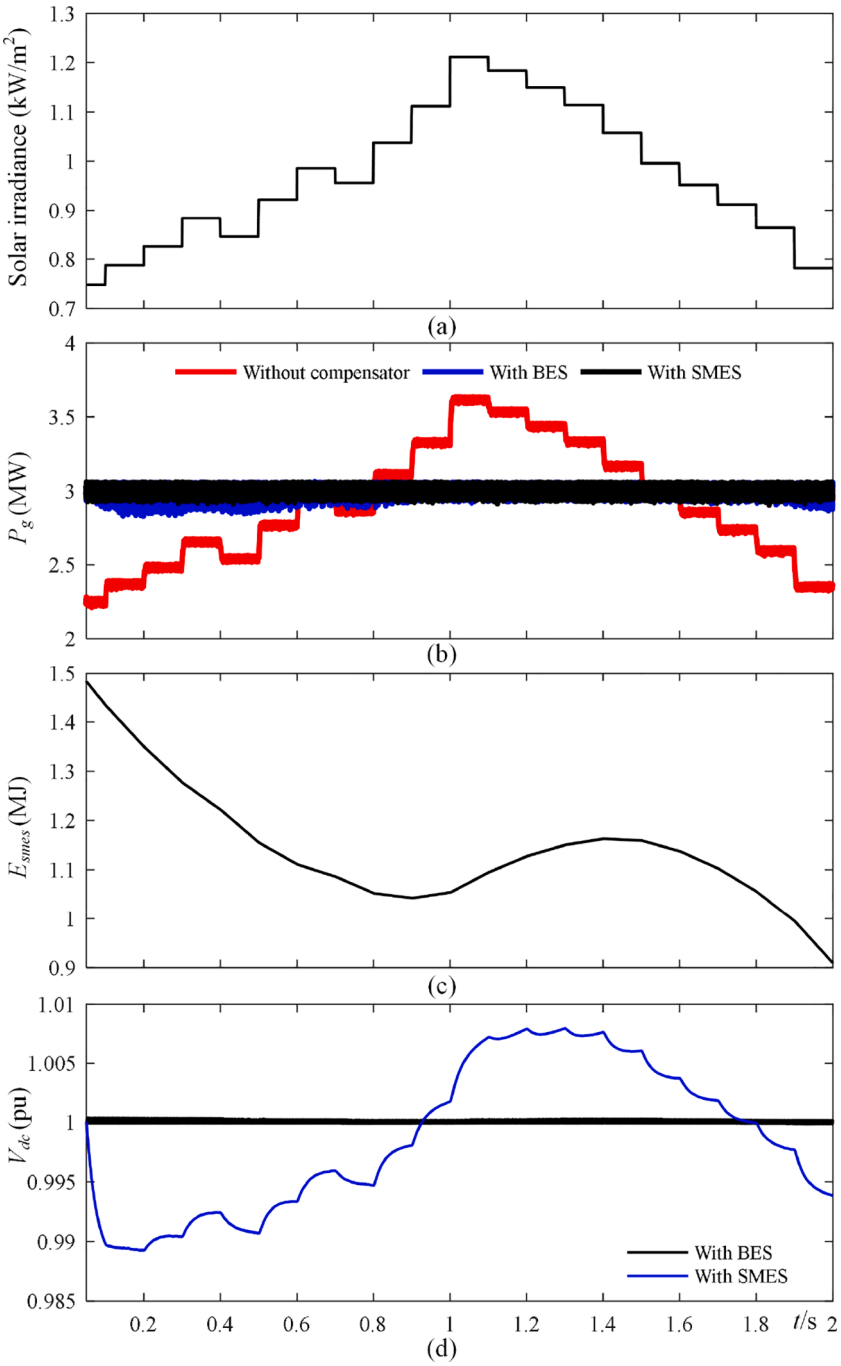


**Fig. 13.** Performance of active power fluctuation suppression between BES and SMES in scenario 3. (a) Simulated solar irradiance curve; (b) Grid side active power; (c) Residual energy storage of SMES; (d) DC-link voltage.

comprehensive performances in four typical scenarios. The parameters of the lead-acid battery are depicted in Table A4.

Scenario 1: Standard solar irradiance condition (1 kW/m$^2$) under nonlinear and unbalanced loads connected, sequentially.
Scenario 2: Standard solar irradiance condition under the pulsating load connected.
Scenario 3: Normal operation condition under time-varying solar irradiance.
Scenario 4: Time-varying solar irradiance condition under nonlinear, unbalanced, and pulsating loads connected, sequentially.

To justify the superiority and robustness of the proposed FLC, a classical PI controller and a sliding mode controller (SMC) are considered to compare the operating performance of the SMES.

### 4.1. Active filtering function

Assume that the nonlinear and unbalanced loads are sequentially connected to the PCC at $t$=0.4 s and $t$=0.7 s. The profiles of grid side voltage and current with no compensator are presented in Fig. 9(a) and (b). As shown in Fig. 9(c), during the period 0.4 ~ 0.7 s, the grid-connected current is distorted with the total harmonic distortion (THD) of 7.29% owing to the injected harmonic and reactive current. The addition of an unbalanced current caused more serious distortion and imbalance during the period 0.7 ~ 1 s.

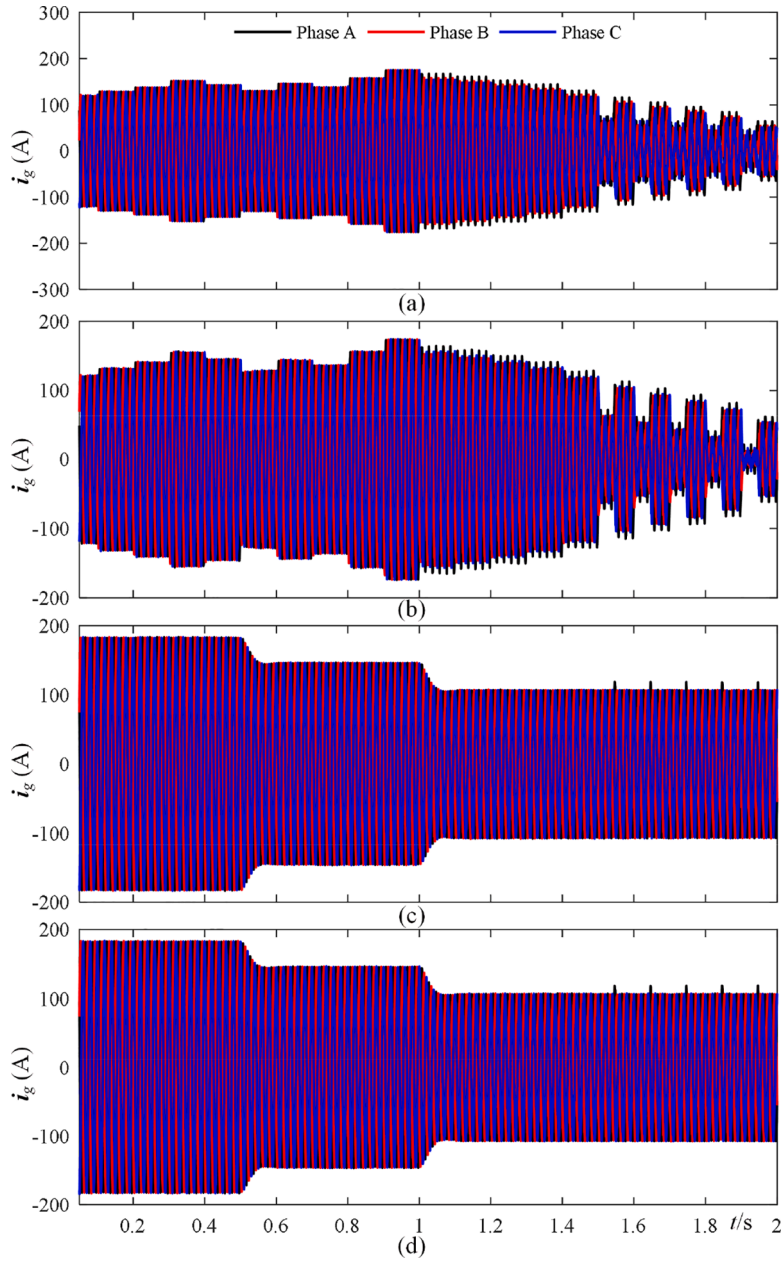


**Fig. 14.** Responses of grid side current with no compensator, SAPF, SAPF-based BES, and SAPF-based SMES in scenario 4. (i) Nonlinear load connected at $t$=0.5 s; (ii) Unbalanced load connected at $t$=1 s; (iii) Pulsating load connected at $t$=1.5 s.

Figs. 10(a) ~ (c) reveal the responses of grid side current with the SAPF, SAPF-based BES, and SAPF-based SMES in scenario 1, respectively. It can be observed that compared with the SAPF, the grid side current shows a symmetrical three-phase sinusoidal waveform with the assistance of ESDs during the period 0.9 ~ 1 s. Moreover, the harmonic spectrograms of the grid side current under the three types of protection devices are shown in Figs. 10(d) ~ (i). During the period 0.4 ~ 0.7 s, all the three protection devices can achieve good filtering performance only for the current distortion caused by the nonlinear load. After the unbalanced current is injected into the grid, the conventional SAPF has been difficult suppressing the nonlinear unbalanced component existing in the grid current with the THD of 9.37%. With the utilization of ESDs, SAPF-based BES and SAPF-based SMES still maintain good active filtering capabilities. However, for the SAPF-based SMES, the grid side current observed is sinusoidal with a better THD of 2.33% during the period 0.7 ~ 1 s.

The profiles of grid side active and reactive power, residual energy storage of the SMES, and DC-link voltage in scenario 1 are presented in Figs. 11(a) ~ (c), respectively. Fig. 11(a) reveals that with the help of ESDs, the grid side active power is smoothly transitioned to a steady-state, and the oscillations resulted from the six times frequency harmonic component and the double frequency negative sequence component are suppressed. In comparison, the SAPF-based SMES behaves more smoothly when an unbalanced load is connected. The SMES discharges to ensure a smooth transition of grid side power, as depicted in Fig. 11(b). As illustrated in Fig. 11(c), since the DC/DC converter is controlled to stabilize the voltage, the SMES DC-link voltage is always maintained at the set value (1 pu) using the proposed FLC method. However, for the SAPF and the SAPF-based BES, the DC-link voltage is fluctuating when the loads are suddenly connected, and there is obvious double frequency oscillation during the period 0.7 ~ 1 s.

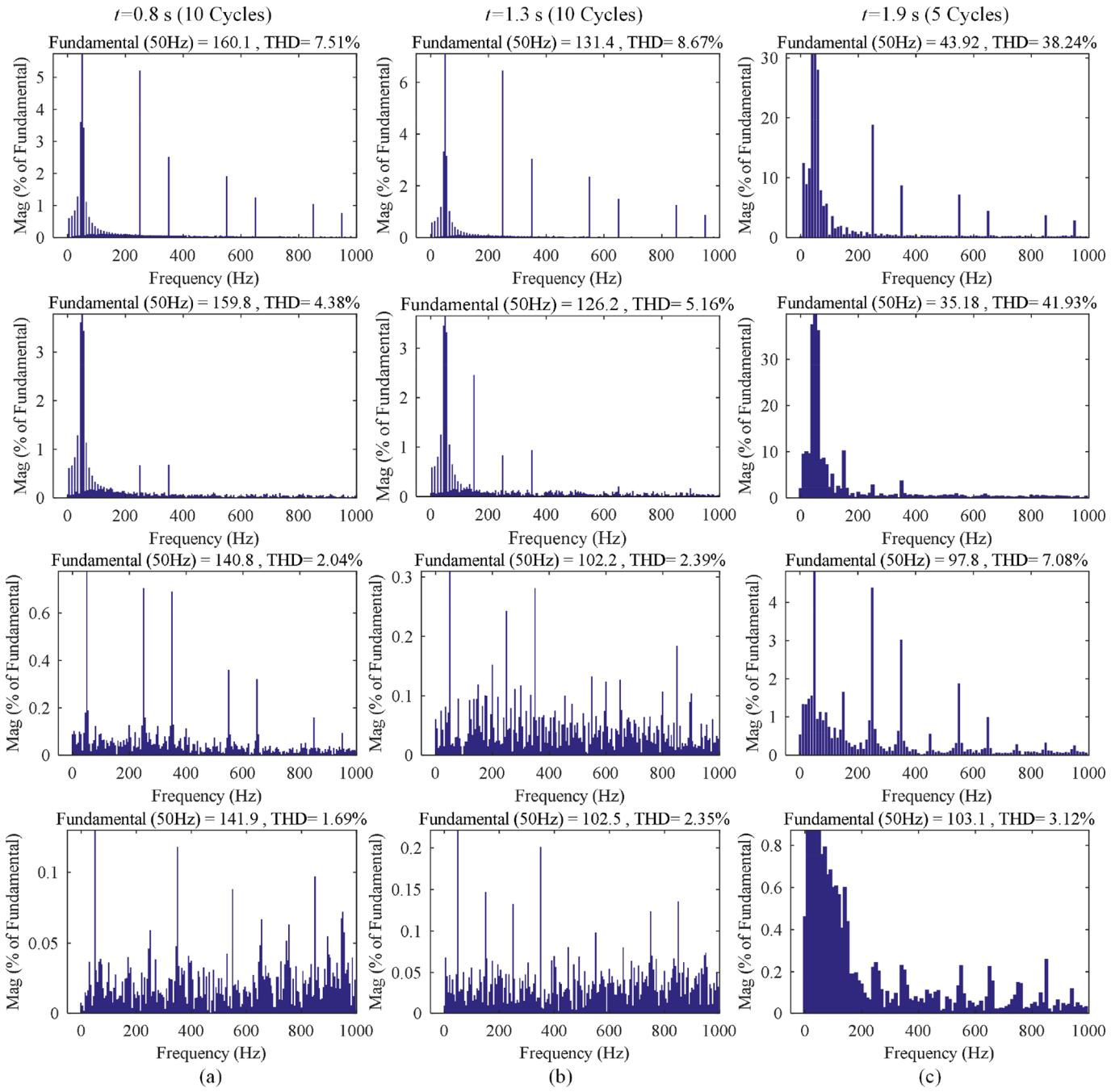


**Fig. 15.** Harmonic spectrum of grid side current with no compensator, SAPF, SAPF-based BES, and SAPF-based SMES. (a) At $t$=0.8 s; (b) At $t$=1.3 s; (c) At $t$=1.9 s.

### 4.2. *Power fluctuation suppression function*

In the grid-connected operation mode, the PV output power is partly caused by pulsating load and random solar irradiance.

Therefore, the power fluctuation suppression function for the SMES is verified in scenarios 2 and 3, respectively.

#### 4.2.1. *Scenario 2*

Assume that the pulsating load with peak active and reactive power demands of 0.5 MW and 0.2 MVAR are connected to the PCC at $t$=0.4 s, as shown in Fig. 12(a). The frequency of the pulsating load is 10 Hz, and the duty cycle is 40%. The simulation results with the BES and SMES in scenario 2 are provided in Figs. 12(b) ~ (d).

Fig. 12(b) shows the responses of grid side active and reactive power with no compensator, BES, and SMES, respectively. It can be clearly observed that the grid side active power is regulated at a constant value of 2.2 MW by injecting additional active power into the grid with ESD. Due to the internal resistance and low-power of lead-acid battery, there will be more dramatic oscillation existing in the grid side active power during the load pulsation compared with the proposed method based on SMES. Moreover, both BES and SMES can mitigate reactive power fluctuation to a constant level (0 VAR). As shown in Fig. 12(c), during the pulsating load fluctuation, the SMES discharges to generate compensation power. Besides, the battery DC-link voltage experiences severe oscillation. In contrast, the DC-link voltage of the SMES is controlled at the constant value, as depicted in Fig. 12(d).

#### 4.2.2. *Scenario 3*

To simplify the simulation, the simulated random solar irradiance data is provided in Fig. 13(a) according to the changing trend of solar

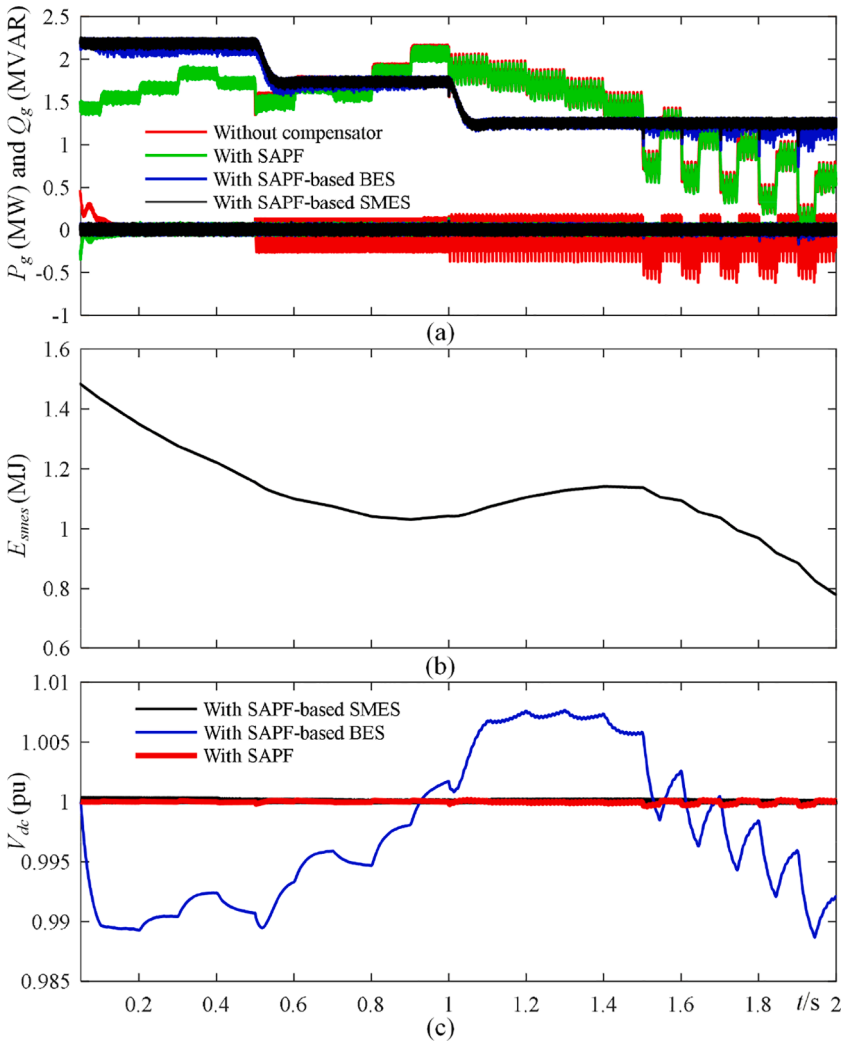


**Fig. 16.** Comparisons among SAPF, SAPF-based BES and SAPF-based SMES in scenario 4. (a) Grid side active and reactive power; (b) Residual energy storage of SMES; (c) DC-link voltage.

irradiance in the daytime. For minimizing output fluctuation, the reference active power demand $P_{pvref}$ should be set to a constant value of 3 MW. The simulation results in scenario 3 are shown in Figs. 13(b) ~ (c).

As illustrated in Fig. 13(b), the PV output power fluctuates drastically under variable solar irradiance. When the PV output power is more than the reference power, the ESDs absorb surplus energy to keep the grid side power at the reference value and vice versa. As depicted, the power fluctuation caused by lower solar irradiance is difficult to smoothly suppressed by the lead-acid battery, which can be eliminated by the SMES. The residual energy of the SMES is shown in Fig. 13(c), which reflects its operation mode in real-time. Fig. 13(d) reveals that frequent charging and discharging operations of lead-acid battery have caused drastic fluctuations in the DC-link voltage, which will severely shorten the service life of the battery.

### 4.3. Comprehensive function

After separately demonstrating the superiority and effectiveness of the single function for the SAPF-based SMES, its comprehensive function is further confirmed in scenario 4. Assume that under variable solar irradiance, the nonlinear, unbalanced, and pulsating loads are connected to the PCC at 0.5 s, 1 s, and 1.5 s, respectively. The simulation results in scenario 4 are shown in Figs. 14(a) ~ (d), Figs. 15(a) ~ (c) and Figs. 16(a) ~ (c).

Figs. 14(a) ~ (d) show responses of the grid side current with no protection device, SAPF, SAPF-based BES, and SAPF-based SMES. The harmonic spectrograms of the grid side current under the four conditions are presented in Figs. 15(a) ~ (c). In the case of grid power fluctuations, the conventional SAPF has lost its good filtering ability. Before the pulsating load is connected, the dynamic performance of the system with the SAPF-based BES and SMES is similar to that in scenario 1. After 1.5 s, the SAPF-based BES has been difficult to constrain harmonic and negative sequence components exiting in the grid side current. However, with the assistant of SAPF-based SMES, only the phase-A current amplitude is suddenly increased to 1.12 times within half a cycle and then promptly maintained stability.

Figs. 16(a) ~ (c) show the profiles of grid side active and reactive power, residual energy of SMES, and DC-link voltage in scenario 4, respectively. Even under extremely complex condition, violent power

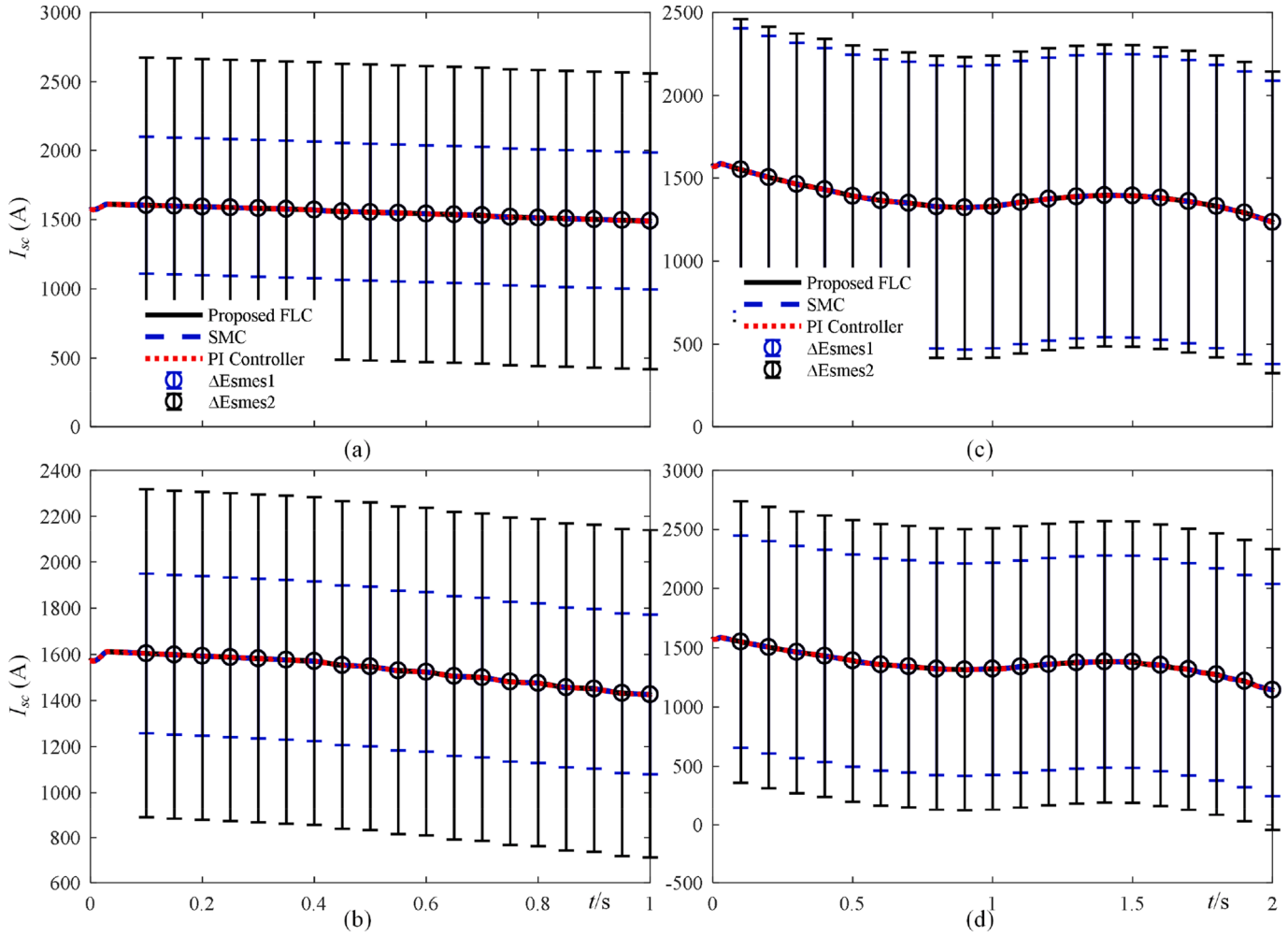


**Fig. 17.** Comparisons among the proposed FLC method, SMC, and PI controller for SC current. (a) In scenario 1; (b) In scenario 2; (c) In scenario 3; (d) In scenario 4.

fluctuations can still be smoothly mitigated using the SAPF-based SMES compared with SAPF and SAPF-based BES. Fig. 16(b) depicts that the residual energy of the SMES is controlled between 10% and 90% of the maximum energy storage capacity. Furthermore, it can be observed that the DC-link voltage remains stable on account of the SMES supplement, as shown in Fig. 16(c).

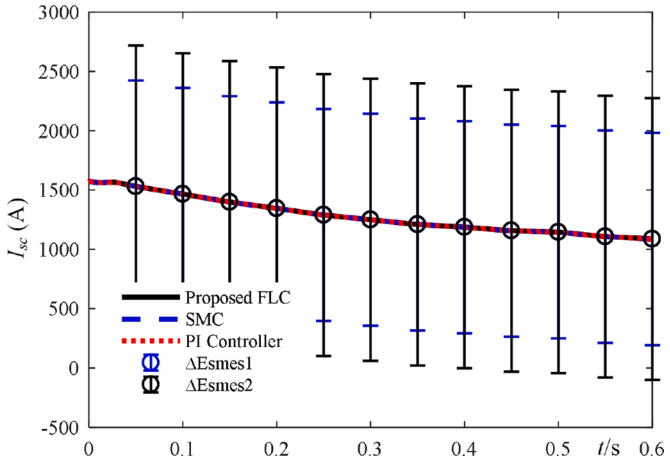


**Fig. 18.** Comparison among the proposed FLC method, SMC, and PI controller for SC current under the partially quenched SC condition in scenario 4.

### 4.4. Comparison with Conventional Method

The comparisons among the proposed FLC method, SMC, and PI controller for SC current in all scenarios mentioned above are carried out, as shown in Figs. 17(a) ~ (d). $\Delta E_{smes1}$ represents the difference between the residual storage energy of the SMES under the proposed FLC and SMC; $\Delta E_{smes2}$ represents the difference between the residual storage energy under the proposed FLC method and the classical PI controller. It can be clearly seen that the proposed FLC method not only stabilizes the DC-link voltage, but also reduces the depth of discharge of the SMES compared with SMC and classical PI controller.

Moreover, an extreme operating condition (Partial SC quench in scenario 4) is considered to verify the robustness of the proposed FLC. The critical current of the SC will decrease as the temperature increases. When the current flowing through the SC exceeds the critical current at the temperature where it is located, the SC will quench, i.e., the SC will have internal resistance. Assuming that the operating temperature of partial SC (One tenth of SC1 and SC3) adopted is increased to 30 K, the critical current $I_c$ and internal resistance $R_{scin}$ of SC1 and SC3 can be estimated as follows [32,42]:

$$I_c = I_{c0}(T) \times G(T,\ B,\ \theta) \tag{23}$$

$$I_{c0}(T) = \begin{cases} (5.92 - 0.065T) \times I_{c0,77K} & T < 75K \\ (3.69 - 0.035T) \times I_{c0,77K} & T > 75K \end{cases} \tag{24}$$

$$G(T,\ B,\ \theta)=\begin{cases}\left[1+\left|\dfrac{B\sin\theta}{B_0(T)}\right|^{\alpha(T)}\right]^{-1} & \theta>\theta_c\\ \left[1+\left|\dfrac{B\sin\theta_c}{B_0(T)}\right|^{\alpha(T)}\right]^{-1} & \theta<\theta_c\end{cases} \tag{25}$$

$$\begin{cases}B_0(T)=0.03+(32-0.393T)\times I_{c0}(T)\times 10^{-4}\\ \alpha(T)=0.2116+0.0083T+(12+0.3T)\times I_{c0}(T)\times 10^{-4}\end{cases} \tag{26}$$

$$R_{scin}=\frac{V_{sc}}{I_{sc}}=SE_c\frac{I_{sc}^{n-1}}{I_c^n} \tag{27}$$

where $I_{c0.77k}=200$ A is critical current at 77 K; $S$ is the length of the quenched SC; $E_c=1$ V/cm; $\theta_c=7.5^{\circ}$ is the misalignment angle of the SC filaments [37].

Fig. 18 illustrates the comparison among the proposed FLC method, SMC, and PI controller for SC current under the partially quenched SC condition in scenario 4. $\Delta E_{smes1}$ and $\Delta E_{smes2}$ are 894.09 J and 1188.30 J on average, reflecting that the proposed FLC controller still has better performance than SMC and PI controller.

## 5. Conclusion

A novel superconducting magnetic energy storage device integrated with active filtering function is presented in this paper. The configuration of the entire system and the control strategies of each converter have been designed. The simulation results show that the utilization of SAPF-based ESD can further improve the active filtering capability of conventional SAPF and also enable it to have active power supply capability.

Compared with SAPF-based BES, the single and comprehensive functions of the SAPF-based SMES are verified to be more effective using the multi-objective control technique and FLC method. The former can thoroughly compensate for the harmonic, reactive, and unbalanced components existing in the grid current, making it restricted within the IEEE-519 standard. The latter can smoothly suppress power fluctuations resulted from load mutation, pulsating load, and time-varying solar irradiance. Meanwhile, the surplus energy of PV generation would be stored in the SC for emergency needs.

In order to prove the superiority and robustness of the proposed FLC, the performance of FLC, SMC, and PI controller are assessed in scenarios 1 ~ 4, and partial SC quench conditions, respectively. The simulation results show that the proposed controller can achieve DC-link voltage stabilization and reduce the depth of discharge of SMES under all operating conditions considered.

The proposed control schemes provide a comprehensive solution for the problems of harmful currents and power fluctuations existing in the PV grid-connected operating microgrid. Moreover, the proposed schemes can also be used to protect sensitive loads and suppress harmonic and unbalanced voltages in island mode. It is expected that the distribution network in the future will be more complex and sensitive. Therefore, the SMES, which can integrate multiple functions, will become the critical alternative to solve the power quality issues.

## CRediT authorship contribution statement

**Jian Xun Jin:** Writing – original draft, Supervision. **Jian Wang:** Methodology, Writing – original draft. **Ruo Huan Yang:** Writing – original draft, Software. **Tian Long Zhang:** Writing – review & editing, Software. **Shuai Mu:** Writing – review & editing. **Ying Jun Fan:** Writing – review & editing. **Yun Qi Xing:** Conceptualization, Funding acquisition.

## Declaration of Competing Interest

The authors declare that they have no known competing financial interests or personal relationships that could have appeared to influence the work reported in this paper.

## Acknowledgements

The current work is partially supported by the Young Scientists Fund of the National Natural Science Foundation of China (Grant No. 51907047), Young Scientists Fund of the Natural Science Foundation of Hebei Province, China (Grant No. E2020202159), Young Program of the Natural Science Foundation of Tianjin, China (Grant No. 20JCQNJC00690), Science and Technology Research Foundation of the Higher Education Institutions of Hebei Province, China (Grant No. QN2019126).

## Appendix

Tables A1–A4.

**Table A1**
Parameters of the PV generation system.

| Parameter | Value |
|---|---|
| Number of PV arrays in parallel | 2 |
| Single PV array maximum power | 1.5 MW |
| PV array side capacitance | 1000 μF |
| Boost inductance | 0.05 mH |
| Inverter DC-link capacitance | 10000 μF |
| *L*-filter inductance | 0.15 mH |
| Rated DC-link voltage | 800 V |
| PI-1 Controller | $K_{op}$=100 $K_{oi}$=5000 |
| PI-2 and PI-3 Controllers | $K_{ip}$=20 $K_{ii}$=5000 |

**Table A2**
Parameters of SMES.

| Parameter | Value |
|---|---|
| SC inductance | 1.193 H |
| SC initial current | 1570 A |
| SC critical current | 1760 A ($T$ = 20 K) |
| Energy capacity | 1.847 MJ |
| Length of the tape usage | 20872 m |
| Rated DC-link voltage | 14.2 kV |
| DC-link capacitance | 10000 μF |
| *L*-filter inductance | 10 mH |

**Table A3**
Parameters of the various loads connected.

| Parameter | | Value |
|---|---|---|
| Balanced load rated active power | | 0.8 MW |
| Nonlinear load | Resistance | 400 Ω |
| | Inductance | 40 mH |
| Unbalanced load | Phase A | 300 + j6.28 Ω |
| | Phase B | 200 + j9.42 Ω |
| | Phase C | 150 + j6.28 Ω |
| Pulsating load | Peak active power | 0.5 MW |
| | Peak reactive power | 0.2 MVAR |

**Table A4**
Parameters of lead-acid battery.

| Parameter | Value |
|---|---|
| Rated voltage | 14.2 kV |
| Rated capacity | 50 Ah |
| Energy capacity | 2556 MJ |
| Initial state-of-charge | 50% |
| Internal resistance | 2.84 Ω |
| Fully charged voltage | 15.4 kV |
| Maximum capacity | 52.08 Ah |

## References


[1] J.T. Bialasiewicz, Renewable Energy Systems with Photovoltaic Power Generators: Operation and Modeling, IEEE Trans. Ind. Electron. 55 (7) (July 2008) 2752–2758.
[2] A. Gholami, M. Ameri, M. Zandi, R.G. Ghoachani, S. Eslami, S. Pierfederici, Photovoltaic Potential Assessment and Dust Impacts on Photovoltaic Systems in Iran: Review Paper, IEEE J. Photovoltaics 10 (3) (May 2020) 824–837.
[3] Om Prakash Mahela, Abdul Gafoor Shaik, Comprehensive Overview of Grid Interfaced Solar Photovoltaic Systems, Renewable Sustainable Energy Rev. 68 (1) (2017) 316–332.
[4] Jackson John Justo, Francis Mwasilu, Ju Lee, Jin-Woo Jung, AC-Microgrids versus DC-microgrids with Distributed Energy Resources: A Review, Renewable Sustainable Energy Rev. 24 (2013) 387–405.
[5] Ken Weng Kow, et al., A Review on Performance of Artificial Intelligence and Conventional Method in Mitigating PV Grid-tied Related Power Quality Events, Renewable Sustainable Energy Rev. 56 (2016) 334–346.
[6] W. Ma, et al., Optimal Allocation of Hybrid Energy Storage Systems for Smoothing Photovoltaic Power Fluctuations Considering the Active Power Curtailment of Photovoltaic, IEEE Access 7 (2019) 74787–74799.
[7] M.H.J. Bollen, et al., Power Quality Concerns in Implementing Smart Distribution-Grid Applications, IEEE Trans. Smart Grid 8 (1) (Jan. 2017) 391–399.
[8] T. Ma, M.H. Cintuglu, O.A. Mohammed, Control of a Hybrid AC/DC Microgrid Involving Energy Storage and Pulsed Loads, IEEE Trans. Ind. Appl. 53 (1) (Jan.-Feb. 2017) 567–575.
[9] Nicu Bizon, Effective Mitigation of The Load Pulses by Controlling the Battery/SMES Hybrid Energy Storage System, Appl. Energy 229 (2018) 459–473.
[10] B. Wang, et al., A Control Strategy for Islanded Three-Phase Inverter with Nonlinear and Unbalanced Loads, in: 2019 IEEE Innovative Smart Grid Technologies – Asia, Chengdu, 2019, pp. 2276–2281.
[11] N. Mendis, K.M. Muttaqi, S. Sayeef, S. Perera, Application of A Hybrid Energy Storage in A Remote Area Power Supply System, in: 2010 IEEE International Energy Conference, Manama, Bahrain, 2010, 576-58.
[12] Gao David Wenzhong, Applications of ESS in Renewable Energy Microgrids. Energy Storage for Sustainable Microgrid, Academic Press, 2015, pp. 35–77.
[13] Reza Hemmati, Hedayat Saboori, Emergence Of Hybrid Energy Storage Systems in Renewable Energy and Transport Applications – A Review, Renewable Sustainable Energy Rev. 65 (2016) 11–23, pp. 11-23.
[14] Z. Zhang, K. Sato, Y. Nagasaki, M. Tsuda, D. Miyagi, T. Komagome, K. Tsukada, T. Hamajima, Y. Ishii, D. Yonekura, Continuous Operation in An Electric and Hydrogen Hybrid Energy Storage System for Renewable Power Generation and Autonomous Emergency Power Supply, Int. J. Hydrogen Energy 44 (41) (2019) 23384–23395.
[15] M.A. Dybko, S.V. Brovanov, Active Power Filter with Battery Energy Storage Based on NPC Inverters, in: 2015 16th International Conference of Young Specialists on Micro/Nanotechnologies and Electron Devices, Erlagol, 2015, pp. 415–421.
[16] B. Singh, S. Kumar, Distributed Incremental Adaptive Filter Controlled Grid Interactive Residential Photovoltaic-Battery Based Microgrid for Rural Electrification, IEEE Trans. Ind. Appl. 56 (4) (July-Aug. 2020) 4114–4123.
[17] D. Somayajula, M.L. Crow, An Integrated Active Power Filter–Ultracapacitor Design to Provide Intermittency Smoothing and Reactive Power Support to the Distribution Grid, IEEE Trans. Sustainable Energy 5 (4) (Oct. 2014) 1116–1125.
[18] Anup Kumar Panda, et al., Design and Modeling of SMES Based SAPF for Pulsed Power Load Demands, Int. J. Electr. Power Energy Syst. 92 (2017) 114–124.
[19] T. Penthia, A.K. Panda, Power Quality Enhancement using Shunt Active Power Filter Integrated with SMES coil, in: 2018 National Power Engineering Conference (NPEC), Madurai, 2018, pp. 1–6.
[20] M.H. Ali, B. Wu, R.A. Dougal, An Overview of SMES Applications in Power and Energy Systems, IEEE Trans. Sustainable Energy 1 (1) (Apr. 2010) 38–47.
[21] Z. Zheng, X. Xiao, X. Chen, C. Huang, L. Zhao, C. Li, Performance Evaluation of a MW-Class SMES-BES DVR System for Mitigation of Voltage Quality Disturbances, IEEE Trans. Ind. Appl. 54 (4) (July-Aug. 2018) 3090–3099.
[22] R.H. Yang, J.X. Jin, Unified Power Quality Conditioner with Advanced Dual Control for Performance Improvement of DFIG-Based Wind Farm, IEEE Trans. Sustainable Energy 12 (1) (Jan. 2021) 116–126.
[23] T. Hamajima, et al., Application of SMES and Fuel Cell System Combined With Liquid Hydrogen Vehicle Station to Renewable Energy Control, IEEE Trans. Appl. Supercond. 22 (3) (June 2012), 5701704-5701704.
[24] Walter Gil-González, Oscar Danilo Montoya, Alejandro Garces, Control of A SMES for Mitigating Subsynchronous Oscillations in Power Systems: A PBC-PI Approach, J. Energy Storage 20 (2018) 163–172.
[25] Oscar Danilo Montoya, Walter Gil-González, Alejandro Garces, Distributed Energy Resources Integration in Single-Phase Microgrids: An Application of IDA-PBC and PI-PBC Approaches, Int. J. Electr. Power Energy Syst. 112 (2019) 221–231.
[26] Walter Gil-González, Oscar Danilo Montoya, Active and Reactive Power Conditioning Using SMES Devices with PMW-CSC: A Feedback Nonlinear Control Approach, Ain Shams Eng. J. 10 (2) (2019) 369–378.
[27] A Rodríguez, F Huerta, EJ Bueno, FJ Rodríguez, Analysis and Performance Comparison of Different Power Conditioning Systems for SMES-Based Energy Systems in Wind Turbines, Energies 6 (3) (2013) 1527–1553.
[28] A.M.S. Yunus, A. Abu-Siada, M.A.S. Masoum, Improving Dynamic Performance of Wind Energy Conversion Systems Using Fuzzy-Based Hysteresis Current-Controlled Superconducting Magnetic Energy Storage, IET Power Electron. 5 (8) (Sep. 2012) 1305–1314.
[29] S.M. Said, M. Aly, B. Hartmann, A.G. Alharbi, E.M. Ahmed, SMES-Based Fuzzy Logic Approach for Enhancing the Reliability of Microgrids Equipped with PV Generators, IEEE Access 7 (2019) 92059–92069.
[30] S.M. Said, H.S. Salama, B. Hartmann, et al., A Robust SMES Controller Strategy for Mitigating Power and Voltage Fluctuations of Grid-Connected Hybrid PV–Wind Generation Systems, Electr. Eng. 101 (2019) 1019–1032.
[31] S.M. Said, A. Ali, B. Hartmann, Tie-line Power Flow Control Method for Grid-connected Microgrids with SMES Based on Optimization and Fuzzy Logic, J. Mod. Power Syst. Clean Energy 8 (5) (Sep. 2020) 941–950.
[32] X.Y. Chen, J.X. Jin, Evaluation of Step-Shaped Solenoidal Coils for Current-Enhanced SMES Applications, IEEE Trans. Appl. Supercond. 24 (5) (Oct. 2014) 1–4.
[33] Boualem Bendib, Hocine Belmili, Fateh Krim, A Survey of the Most Used MPPT Methods: Conventional and Advanced Algorithms Applied For Photovoltaic Systems, Renewable Sustainable Energy Rev. 45 (2015) 637–648.
[34] F. Karbakhsh, G.B. Gharehpetian, J. Milimonfared, A. Teymoori, Three Phase Photovoltaic Grid-Tied Inverter Based on Feed-Forward Decoupling Control Using Fuzzy-PI Controller, in: 2016 7th Power Electronics and Drive Systems Technologies Conference (PEDSTC), Tehran, 2016, pp. 344–348.
[35] J.X. Jin, et al., HTS Power Devices and Systems: Principles, Characteristics, Performance, and Efficiency, IEEE Trans. Appl. Supercond. 26 (7) (Oct. 2016) 1–26.
[36] P. Mukherjee, V.V. Rao, Effective Location of SMES for Power Fluctuation Mitigation of Grid Connected Doubly Fed Induction Generator, J. Energy Storage 29 (2020).
[37] T. Nakashima, S. Kobayashi, T. Kagiyama, K. Yamazaki, M. Kikuchi, S. Yamade, K. Hayashi, K. Sato, G. Osabe, J. Fujikami, Overview of the Recent Performance of DI-BSCCO Wire, Cryogenics 52 (12) (2012) 713–718.
[38] S. Khadidja, M. Mountassar, B. M'hamed, Comparative Study of Incremental Conductance and Perturb & Observe MPPT Methods for Photovoltaic System, in: 2017 International Conference on Green Energy Conversion Systems (GECS), Hammamet, 2017, pp. 1–6.
[39] R.S. Herrera, P. SalmerÓn, H. Kim, Instantaneous Reactive Power Theory Applied to Active Power Filter Compensation: Different Approaches, Assessment, and Experimental Results, IEEE Trans. Ind. Electron. 55 (1) (Jan. 2008) 184–196.
[40] V.T. Doan, K.Y. Kim, W Choi, D.W. Kim, Design of a Hybrid Controller for the Three-phase Four-leg Voltage-source Inverter with Unbalanced Load, J. Power Electron. 17 (1) (Jan. 2017) 181–189.
[41] J. Tong, J. Qiao, L. Liu, C. Fan, X. Li, F. Li, Optimization of APF Single Hysteresis SVPWM Current Tracking Control Strategy, in: 2018 IEEE 3rd Advanced Information Technology, Electronic and Automation Control Conference (IAEAC), Chongqing, 2018, pp. 98–102.
[42] Jianxun Jin, Runtao Zhang, Zhiwei Lin, Youguang Guo, Jianguo Zhu, Xiaoyuan Chen, Boyang Shen, Modelling Analysis of Periodically Arranged High-Temperature Superconducting Tapes, Physica C: Supercond. Appl. 578 (2020).